Article

First-Principles Calculations of Luminescence Spectra of Real-Scale Quantum Dots

Sungwoo Kang, Seungwu Han,* and Youngho Kang*

Cite This: *ACS Mater. Au* 2022, 2, 103−109
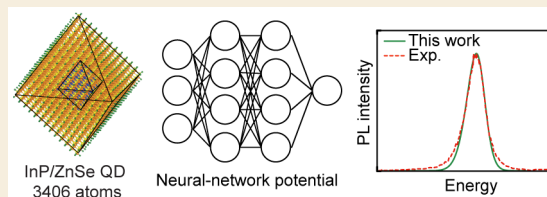
Read Online

ACCESS | 📊 Metrics & More | 📖 Article Recommendations | 🆂🅸 Supporting Information

ABSTRACT: The luminescence line shape is an important feature of semiconductor quantum dots (QDs) and affects performance in various optical applications. Here, we report a first-principles method to predict the luminescence spectrum of thousands of atom QDs. In our approach, neural network potential calculations are combined with density functional theory calculations to describe exciton−phonon coupling (EPC). Using the calculated EPC, the luminescence spectrum is evaluated within the Franck−Condon approximation. Our approach results in the luminescence line shape for an InP/ZnSe core/shell QD (3406 atoms) that exhibits excellent agreement with the experiments. From a detailed analysis of EPC, we reveal that the coupling of both acoustic and optical phonons to an exciton are important in determining the spectral line shapes of core/shell QDs, which is in contrast with previous studies. On the basis of the present simulation results, we provide guidelines for designing high-performance core/shell QDs with ultrasharp emission spectra.

KEYWORDS: *Quantum dot, Luminescence line shape, Machine learning, Neural network potential, Exciton−phonon coupling*

1. INTRODUCTION

Over the past decades, semiconductor quantum dots (QDs) have emerged as promising materials for optical devices. A unique feature of QDs is the tunable band gap enabled by quantum confinement effects. As a result, the emission wavelength can be readily controlled by synthesizing QDs of different sizes. Furthermore, exciton wave functions can be confined within a single particle, enabling high luminescence efficiency if the generation of surface traps are sufficiently suppressed during synthesis. Because of these advantages, QDs are garnering considerable attention in applications in biological imaging, lasers, and wide-color gamut displays.[1−3]
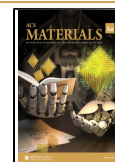
To fully realize the potential of QDs in various applications, QDs need to exhibit a high spectral purity. Therefore, many efforts have been made to reduce the luminescence line width of QDs. There are two major sources, namely, inhomogeneous and homogeneous, that affect the emission line width of a QD ensemble. The inhomogeneous source arises from the nonuniformity of the QD size in a batch that causes a distribution of emission wavelengths of the particles.[4] However, owing to recent progress in synthetic methods, QD batches can be produced with high size uniformity. For instance, the luminescence spectra of CdSe QD samples can exhibit line widths close to the single-dot level at present.[5] In the case of InP/ZnSe QD batches, the small size deviation of ~2 Å was reported.[6] On the other hand, spectral dynamics, exciton fine structures, and exciton−phonon coupling (EPC) in an individual QD are homogeneous sources. Among them, EPC is known to predominantly determine the line width of a single QD at room temperature.[7−10] Because EPC is intrinsic

(namely, unavoidable), it is crucial to design QDs to minimize EPC to obtain sharp luminescence spectra.

The foregoing discussion highlights the importance of understanding the microscopic origin of EPC and its impacts on the luminescence spectrum in QDs, but this understanding has yet to be established. One of the long-standing issues related to EPC in QDs is the relative importance of acoustic and optical phonons. Several groups have investigated which phonon modes (acoustic versus optical modes) dominantly couple with an exciton in QDs.[9−12] However, the conclusions from previous works were inconsistent. On the other hand, the incomplete understanding of EPC has interrupted the clear interpretation of experimental results, leading to ambiguities. For example, previous experiments showed that the single-dot spectral line width of CdSe cores is initially suppressed upon shell growth because of the removal of dangling bonds.[9] However, further shell growth widens the line width. The broader peaks at thicker shells were attributed to the enhanced EPC, but the specific origin has not yet been clarified.

Theoretical investigation of QDs using density functional theory (DFT) calculations can provide important insights into EPC that are difficult to obtain by experiments alone. In a previous study, we reported an *ab initio* method to evaluate the

luminescence line shapes of QDs due to EPC, combining the DFT and Franck−Condon approximation.[13] We applied the method to CdSe core-only QDs and identified the intrinsic limit of the line width. Although the method is accurate and reliable, its application is practically limited to small QDs, including a few hundred atoms, because of the high computational costs of DFT calculations. Therefore, an alternative approach is necessary to investigate the line shape of technologically relevant core/shell QDs that consist of thousands of atoms or more.[6,14,15] Classical molecular dynamics (MD) simulations based on machine-learning interatomic potentials,[16−18] such as neural network potential (NNP), may suggest a solution to handling such large systems. This approach allows us to examine structural properties with a much lower computational cost than DFT while maintaining the DFT accuracy. Indeed, MD using NNP was successfully applied to study phase-change materials[19] and metal−semiconductor interfaces[20] at large scales and search equilibrium crystal structures of inorganic materials.[21]

In this work, we demonstrate that an *ab initio* method combining DFT and NNP is successful in describing the EPC of thousands of atom QDs at a modest computational cost. In our approach, NNP is used to calculate the ground-state atomic configuration and vibrational spectrum of a QD, which are the most time-consuming parts, while DFT is used to describe an exciton state. The results from the NNP and DFT calculations are then employed to calculate EPC, which is defined in terms of Huang−Rhys (HR) factors. The developed method is thoroughly validated by comparing the results with those from the full DFT calculations. On the other hand, using calculated HR factors, we obtain a spectral line shape of QDs within the Franck−Condon approximation. With the example of an InP/ZnSe core/shell QD, which has recently emerged as an eco-friendly and efficient light emitter, we show that our methodology closely reproduces experimental line shapes. To the best of our knowledge, this is the first work to predict luminescence line shapes of real-size QDs without any empirical information. We also analyze HR factors in InP core-only and InP/ZnSe core/shell QDs. This reveals that exciton−acoustic phonon coupling dominates the line width in the InP core-only QD. Meanwhile, the introduction of the ZnSe shell causes the frontier molecular orbitals of the InP core to leak unevenly into the shell region. This amplifies the coupling of optical modes to an exciton, further increasing the line width. On the basis of the insights from our calculations, we provide strategies to achieve narrow line widths for core/shell QDs.

2. METHODS

2.1. Luminescence Spectrum

We calculate the spectral line shape based on the Franck−Condon approximation, where the electronic transition probability is assumed to be independent of atomic coordinates.[13] In this approximation, the normalized luminescence intensity $[I(\omega)]$ can be expressed as $I(\omega) = C\omega^3 A(\omega)$, where ω and C denote the photon frequency and normalization constant, respectively. A spectral function $A(\omega)$ is responsible for the broadening of a spectral line shape due to phonon transitions during optical emission and is given by[22]

$$A(\omega) = \sum_{\{l_k\}} \left[\prod_k \sum_m w_{km}(T) \left| \langle \chi^g_{k(m+l_k)} | \chi^e_{km} \rangle \right|^2 \right]$$
$$\times \delta\left(E_{ZPL} - \sum_k l_k \hbar\omega_k - \hbar\omega \right) \quad (1)$$

where E_{ZPL} is the energy of the zero-phonon line and $\chi^g_{k(m+l_k)}$ and χ^e_{km} are phonon wave functions of the ground and excited states, respectively. k is the index for the phonon mode, and m and $(m + l_k)$ are the excitation numbers for each mode. $\{l_k\}$ indicates that a possible set of different combinations of l_k and $w_{km}(T)$ is the thermal occupation of χ^e_{km} at a given temperature T.

The direct calculation of eq 1 requires sophisticated multidimensional integrals of $\langle \chi^g_{k(m+l_k)} | \chi^e_{km} \rangle$, which are computationally prohibitive for thousands of atom QDs. Instead of calculating them explicitly, one can employ the parallel approximation where vibrational wave functions are assumed to be identical in both the excited and ground states.[23] In the parallel approximation, the overlap between two vibronic wave functions is expressed in terms of a simple parameter called the Huang−Rhys (HR) factor as follows

$$\sum_m w_{km}(T) \left| \langle \chi^g_{km} | \chi^e_{k(m+l_k)} \rangle \right|^2$$
$$= \exp\left\{ \frac{l_k\hbar\omega_k}{2k_bT} - S_k \coth\left(\frac{\hbar\omega_k}{2k_bT}\right) \right\} I_{l_k}\left\{ S_k / \sinh\left(\frac{\hbar\omega_k}{2k_bT}\right) \right\} \quad (2)$$

where k_b and I_{l_k} are the Boltzmann constant and modified Bessel function, respectively. S_k is the partial HR factor of the kth phonon mode, which is defined as

$$S_k = \frac{\omega_k q_k^2}{2\hbar} \quad (3)$$

where q_k is the projection of the structural variation during the vertical transition onto the vibrational mode. Within the harmonic approximation, q_k can be computed as[24,25]

$$q_k = \sum_\alpha \frac{1}{\omega_k^2 m_\alpha^{1/2}} [\vec{F}_e(\alpha) - \vec{F}_g(\alpha)] \cdot \vec{n}_k(\alpha) \quad (4)$$

In eq 4, m_α is the mass of atom α and $\vec{n}_k(\alpha)$ is the normalized phonon eigenvector. $\vec{F}_g(\alpha)$ $(\vec{F}_e(\alpha))$ is the force acting on atom α at the ground (excited) state when every atomic position is fixed at the ground state. On the other hand, calculations of eq 1 considering all the phonon modes are still computationally demanding. This issue can be addressed by adopting an effective vibrational mode with the frequency (ω_{eff}) given by[23]

$$\omega_{eff}^2 = \sum_k \frac{q_k^2}{\sum_k q_k^2} \omega_k^2 \quad (5)$$

where $q_k^2/\sum_k q_k^2$ represents a partial contribution of the kth mode to the structural change during the optical transition. The effective Huang−Rhys factor for this effective mode is then calculated as

$$S_{eff} = \frac{\sum_k S_k \hbar\omega_k}{\hbar\omega_{eff}} \quad (6)$$

To compute the luminescence spectrum through eqs 1−6, we need information on the atomic configuration and vibrational spectrum at the ground state. We obtain them by NNP calculations. On the other hand, $\vec{F}_e(\alpha) - \vec{F}_g(\alpha)$ in eq 4 is evaluated using DFT on the NNP-optimized structure. We refer to this approach as NNP+DFT. The δ function in eq 1 is replaced with a Gaussian distribution with a smearing width of 10 meV, which is much smaller than the full width of half-maximum (FWHM) of the line shapes (see below). We also tested smaller (5 meV) and larger (20 meV) smearing widths, which changed the FWHM by only approximately ±5% (see Figure S1).

2.2. DFT Calculations

All DFT calculations in the present work are performed by using Vienna Ab-initio Simulation Package (VASP) code. The cutoff energy for the plane wave basis is set to 450 eV except for a $(InP)_{95}(ZnSe)_{1283}H_{650}$ QD, for which the smaller cutoff energy of 210 eV is chosen through careful tests of the calculation results for EPC and line shape (see Figure S2). The atomic geometries are optimized until forces acting on every atom are less than 1 meV/Å. We employ the generalized gradient approximation (GGA) functional with Hubbard U corrections.[26,27] The effective on-site energy $(U−J)$ for In 4d and Zn 3d states are set to 5 and 10 eV, respectively. These values of $U−J$ yield results consistent with those from more accurate hybrid functional[28] calculations (Table S1). The calculated lattice parameters, effective masses, and dielectric constants of bulk InP and ZnSe are in good agreement with the experimental results (Tables S2−S4). The vibrational modes are calculated by a finite-difference method. We use the constrained DFT method to simulate an exciton state.[29,30] Because the line shape is insensitive to spin configurations, as shown in Figure S2 and ref 13, we conducted nonspin-polarized calculations. When emulating the exciton state, the degenerate highest occupied molecular orbitals (HOMOs) of the InP core are evenly emptied. The Zn (Se) surface atoms of ZnSe and InP/ZnSe QDs are passivated by pseudohydrogen atoms with a charge of $1.5e^−$ $(0.5e^−)$, and In (P) surface atoms of InP QDs are passivated by pseudohydrogen atoms with a charge of $1.25e^−$ $(0.75e^−)$. The mass of pseudohydrogen atoms is set to 63.546 amu, similar to that of Zn, but a change in the pseudohydrogen mass rarely affects the calculation results.[13] Phonon spectra were obtained by using the Phonopy package.[31]

2.3. NNP Training and NNP Calculations

NNP is trained using the SIMPLE-NN code.[32,33] We adopt the Behler-type NNP, which reproduces the DFT energy as a sum of atomic energies.[16] The structure of the neural network is 256−60−60−1 with atom-centered symmetry functions[34] as input layers. The cutoff distance of the symmetry functions is set to 7 Å. We transform symmetry function vectors by principal component analysis to avoid a strong correlation between the components of the symmetry functions, and all the components are normalized. The training procedure minimizes the loss function defined by the sum of energy, force, and stress errors and the L2 regularization term. One-fifth of the reference data generated for training NNP is randomly chosen and used as a validation set. The weights of the network are optimized using the ADAM optimization method[35] with a batch size of 12. The LAMMPS package is employed for NNP calculations.[36] Vibrational modes are calculated by using the PhonoLAMMPS code.[37]

3. RESULTS AND DISCUSSION

3.1. NNP for InP/ZnSe Core/Shell QDs

We develop NNP for InP/ZnSe core/shell QDs. Figure 1a shows the atomic structure and cross section of the QD model $[(InP)_{95}(ZnSe)_{1283}H_{650}]$, which is analogous to QDs in the experiments.[38−40] For simplicity, we consider the octahedral shape with the InP(111)/ZnSe(111) interface and ZnSe(111) surface. The structure of the core/shell QD can be characterized by four different parts: InP bulk, ZnSe bulk, InP/ZnSe interface, and ZnSe surface. Thus, reference geometries for training NNPs are generated from trajectories of DFT-based MD simulations of bulk, surface, and interface models (Figure 1b) at 400 and 1000 K. In addition, MD trajectories at 300 K of small ZnSe core-only and InP/ZnSe core/shell QD models are included in the training set to improve the accuracy of NNP for the description of vertex and edge structures of the core/shell QD. Detailed information on the training set is presented in Table S5. The total root-mean-square errors (RMSEs) of energy, force, and stress for the validation set are 1.5 meV, 70 meV/Å, and 2.3 kbar,
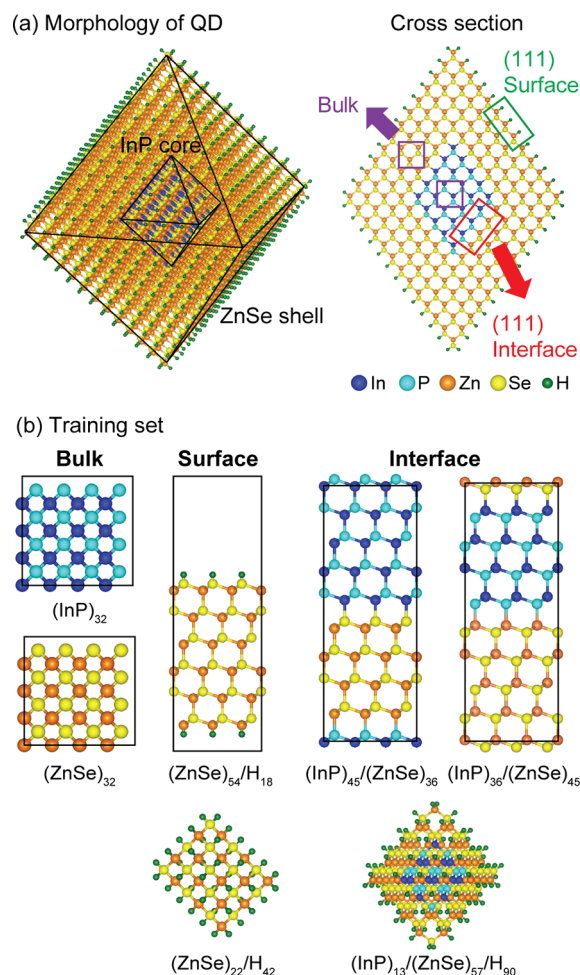

Figure 1. (a) Computational model of an InP/ZnSe QD $[(InP)_{95}(ZnSe)_{1283}H_{650}]$ and (b) the atomic models used to generate the training set for NNP.

respectively. These RMSEs are small and comparable with NNP models for other materials,[41−43] confirming that the NNP is successfully trained. We confirm that overfitting does not occur during the training (Figure S3).

To validate the developed NNP, we calculate the equation of states of the bulk phases of InP and ZnSe using NNP calculations (green lines in Figure 2a,b, respectively). The results are in good agreement with those of DFT. In addition, we also show in Figure 2c,d that NNP successfully reproduces the phonon spectra of InP and ZnSe obtained by DFT. Compared to the experiments, both NNP and DFT slightly underestimate the frequencies of the optical modes (Figure 2c,d). However, the consideration of the experimental frequencies rarely changes the emission line shape compared to that obtained using the calculated frequencies because the frequency difference between the experiment and theory is marginal (Figure S4). Thus, below, we calculate line shapes using calculated frequencies.

Next, to check the accuracy of the NNP+DFT approach in describing EPC, we compare the EPC results from NNP+DFT and the full DFT calculations for two QD models: ZnSe QDs $(Zn_{44}Se_{40}H_{64})$ and InP/ZnSe QDs $[(InP)_{22}(ZnSe)_{73}H_{110}]$. In this comparison, the QD models are chosen to be larger than those included in the training set to demonstrate that NNP+DFT is applicable to QDs of any size. The atomic structures
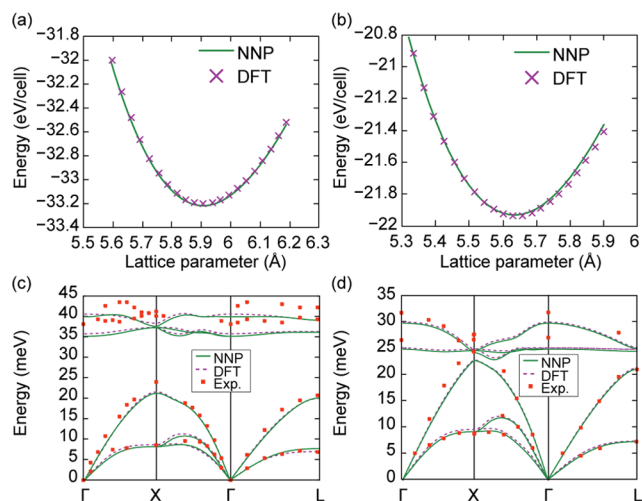
Figure 2. (a, b) The equation of states and (c, d) phonon dispersion curves for (InP, ZnSe) calculated by NNP compared with those calculated by DFT and the experiment (InP: ref 44; ZnSe: ref 45).

3.2. Luminescence Spectrum of InP/ZnSe Core/Shell QD

Now that we have validated the NNP+DFT method, we apply it to the real-scale core/shell QD model, namely, (InP)$_{95}$(ZnSe)$_{1283}$H$_{650}$, as shown in Figure 1a. The model has a core radius (r_{InP}) of 0.95 nm and a shell thickness (t_{ZnSe}) of 1.45 nm. Here, r_{InP} (r_{total}) is defined as the average distance from the center of the QD to In and P (Zn and Se) atoms at the interface (surface), and t_{ZnSe} is defined as $r_{total} - r_{InP}$. These dimensions of the QD model are comparable to InP/ZnSe/ZnS QDs in the experiments (r_{InP} = 1 nm, t_{ZnSe} = 1.5 nm, and t_{ZnS} = 0.5 nm).[38−40] Note that the outer ZnS shell in the experiments, which is not considered in our calculations, serves only as a defect passivation layer for the ZnSe surface (like hydrogen atoms in our model) and rarely affects the physical properties of the InP core.[39] Figure 4a shows the calculated line shape for the InP/ZnSe QD at room temperature based on the EPC from NNP+DFT, along with experimental data that were measured by single-dot photoluminescence (PL) spectroscopy. The agreement between the calculation and the experiment is excellent. In Figure 4b, we also show that our calculations well reproduce the experimental temperature dependence of the line width. (Because the experimental data in Figure 4b are ensemble line widths that are affected by temperature-independent inhomogeneous sources, we compare the relative line widths with respect to the values at 78 K.) These favorable comparisons between theory and experiment attest to the predictive power of our methodology.

The analysis of EPC in the InP/ZnSe core/shell QD can provide important insights into the spectral broadening that may help optimize the core/shell structure. We present the distribution of partial HR factors for an InP core-only QD (In$_{95}$P$_{95}$H$_{110}$; r_{InP} = 0.95 nm) (Figure 5a) and the InP/ZnSe core/shell QD (Figure 5b). The data for the InP core-only QD is obtained by the full DFT calculations. In Figure 5a, we see that the HR factors for phonons below 10 meV are particularly pronounced in the InP core-only QD. This indicates the strong coupling between the exciton and acoustic phonons. The dominance of acoustic modes in the EPC is attributed to the antibonding character of the lowest unoccupied molecular orbital (LUMO) of InP; the occupation of the LUMO in the
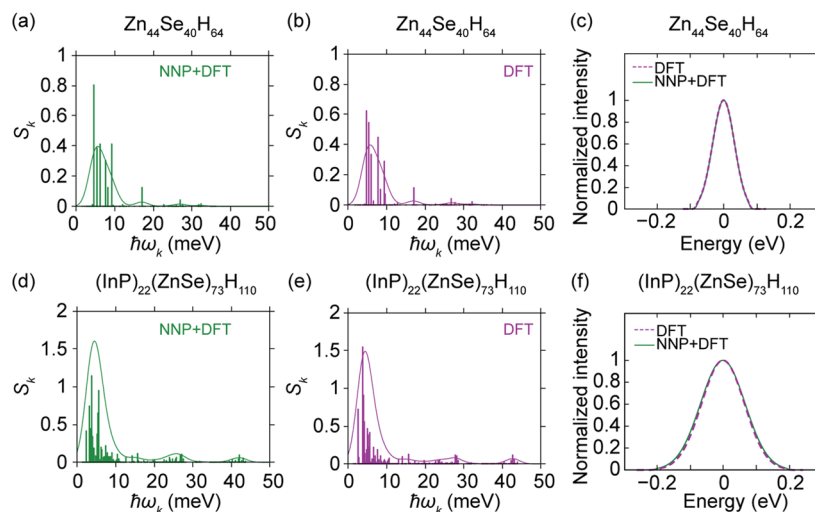
of the models are presented in Figure S5, and the temperature is set to 300 K. As shown in Figure 3a,b, the overall distributions of partial HR factors of the ZnSe QDs are consistent between NNP+DFT and DFT. The slight difference of each S_k between the two calculations occurs because of a subtle difference in the equilibrium structures, which results in a dissimilar projection efficiency for a given phonon mode (i.e., q_k). However, the natures of the EPC described by both methods are essentially the same, as inferred by the similar distributions of the HR factors. In addition, the two approaches yield almost identical luminescence line shapes (Figure 3c). (In Figure 3c, the peak position, i.e., E_{ZPL}, is set to 0 eV.) Similar to the ZnSe QDs, we find good agreement of the frequency dependence of partial HR factors between the NNP+DFT (Figure 3d) and DFT (Figure 3e) calculations for the core/shell InP/ZnSe QD model. Figure 3f also shows that the line shape for the core/shell QD based on NNP+DFT results is favorably compared to that obtained from DFT.

Figure 3. Partial HR factors calculated by (a, d) NNP+DFT and (b, e) DFT and (c, f) luminescence spectra calculated on the basis of HR factors from NNP+DFT and DFT for (ZnSe, InP/ZnSe) QDs. In a, b, d, and e, the vertical lines represent the partial HR factor for each mode, which is smeared (σ = 1.7 meV) into a continuous envelope. The peak positions in c and f are set to zero.
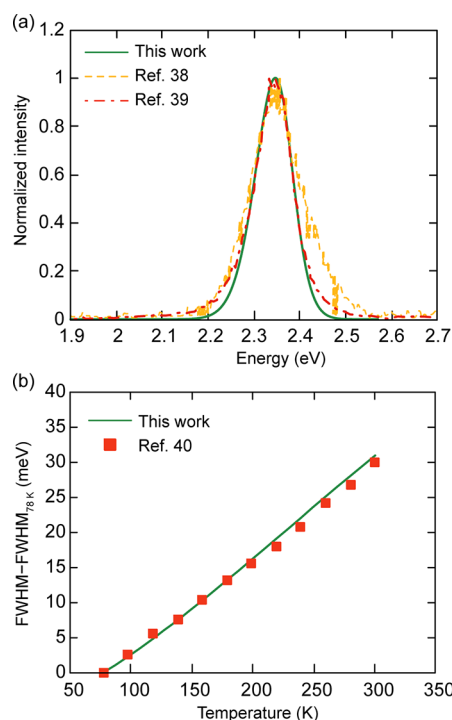
Figure 4. (a) Calculated and experimental luminescence spectra and (b) temperature dependence of the line widths for InP/ZnSe core/shell QDs. The $(InP)_{95}(ZnSe)_{1283}H_{650}$ model is used to obtain the calculation data, and the experimental results are for QDs with similar sizes (see the main text). The experimental results are obtained from refs 38−40.

Figure 5. Partial Huang−Rhys factors of (a) $(InP)_{95}H_{110}$ and (b) $(InP)_{95}(ZnSe)_{1283}H_{650}$ calculated by NNP+DFT and DFT, respectively. The linear charge density of the LUMO (e^-) and HOMO (h^+) of (c) $(InP)_{95}H_{110}$ and (d) $(InP)_{95}(ZnSe)_{1283}H_{650}$ along the $\langle 111 \rangle$ direction from the center of the QD. Mode-resolved line widths for (e) $(InP)_{95}H_{110}$ and (f) $(InP)_{95}(ZnSe)_{1283}H_{650}$.

excited state leads to the expansion of the lattice that involves the atomic motion associated with acoustic modes. Strong exciton−acoustic phonon coupling was also reported for CdSe core-only QDs.[13]

In contrast to the InP core-only QD, the optical modes of both the core ($\hbar\omega \sim 40$ meV) and shell ($\hbar\omega \sim 25$ meV) moderately couple with an exciton in the InP/ZnSe QD (Figure 5b). This larger exciton−optical phonon coupling in the core/shell structure results from uneven leakage of the frontier molecular orbitals of InP into the ZnSe shell. Specifically, in the core-only QD, the HOMO and LUMO of InP are confined in a similar area (Figure 5c), while the LUMO is more spread out into the shell area than the HOMO in the core/shell QD (Figure 5d). As a result of the separation of the HOMO and LUMO, electronic polarization occurs in the core−shell QD, which enhances exciton−optical phonon coupling and results in a wider line shape (FHMW of 97 meV) compared to that of the core-only QD (FHMW of 72 meV) (Figure S6). This leakage-induced polarization would be one of the reasons for wider line shapes of the core/shell QDs at thicker shells in the experiments.[8] In passing, the core-only QD considered in the present work has no defects, and thus, the calculated line width should be regarded as the lowest limit. In experiments, core-only QDs usually contain dangling bonds on the surface to some extent even if molecular ligands are attached to the surface for passivation, and such defects can broaden the line width because of polarization effects.[10,13]

To unveil the phonon mode (acoustic versus optical) that dominantly contributes to the spectral line shapes of QDs, we examine the mode-resolved line widths for the core-only (Figure 5e) and core/shell QDs (Figure 5f) by limiting the
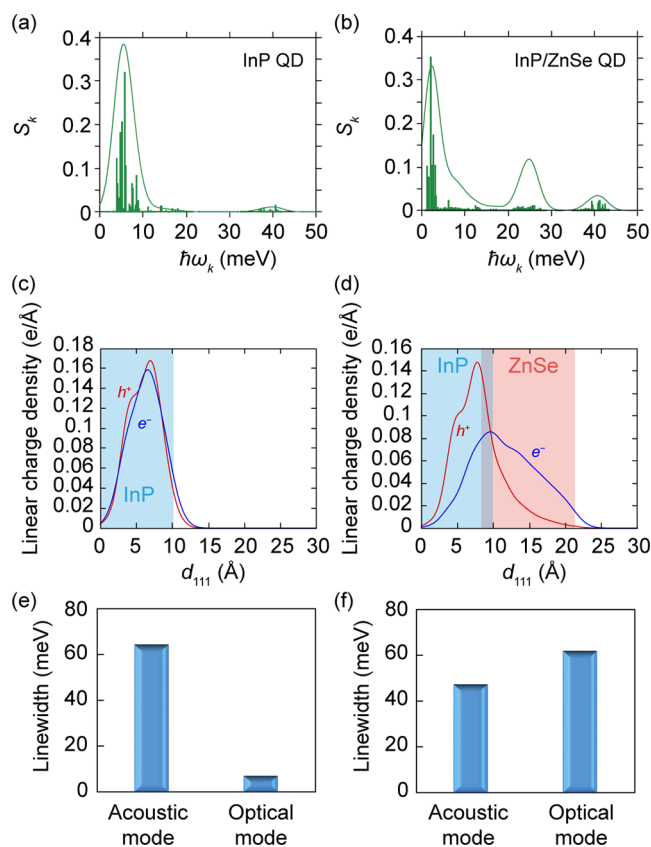
phonon index to a certain mode during the calculation of the line shape. We consider phonons with frequencies smaller than 20 meV to be acoustic modes, while the others are optical modes based on phonon spectra in Figure 2c,d. We confirm that the lattice mismatch between InP and ZnSe marginally changes vibrational frequencies of each material in the QD compared to that of the corresponding bulk (see Figure S7). Although frequencies of acoustic modes of InP and ZnSe can slightly exceed 20 meV, low-frequency modes among acoustic phonons (<10 meV) dominate the exciton−phonon coupling, as seen in Figure 5a,b. Therefore, a slight change in the separation criterion for acoustic and optical phonons barely affects the relative contribution to the line width. Each sum of the partial line widths in Figure 5e,f is not exactly identical with the corresponding total line width because of the nonlinearity of eq 1. However, the results can qualitatively reflect the impacts of the respective phonon mode on the line width. As we discussed above, exciton−acoustic phonon coupling dominates the line shape for InP core-only QDs. Interestingly, in the InP/ZnSe QDs, the EPCs for both acoustic and optical phonons similarly contribute to the line width. This finding is in contrast to previous studies that emphasize the role of a certain mode between optical and acoustic phonons.[8,10,11] Note that the contribution of optical modes to the line width can be similar to that of acoustic modes due to larger phonon frequencies (see eq 2) despite smaller HR factors.

On the basis of our results, we suggest strategies to design core/shell QDs to achieve ultrasharp line width. First, a core material in which frontier molecular orbitals have weak bonding and antibonding combinations between constituting elements would be advantageous to reduce exciton–acoustic phonon coupling, thereby decreasing the spectral broadening. Second, as shown for the InP/ZnSe QD, it is crucial to prevent uneven distribution of frontier molecular orbitals of a core material for a core/shell structure. This may be accomplished by selecting a shell material that yields a proper band offset. For example, in the case of the InP core, the LUMO tends to spill into the shell area more than the HOMO, which can be deduced by the lighter effective mass of the former. Thus, a shell material that leads to a larger band offset between LUMOs than between HOMOs while maintaining the type-1 band alignment will help reduce the line width.

4. CONCLUSION

In summary, we demonstrated that the NNP+DFT method, combined with the Franck–Condon approximation, can be an effective tool to predict experimental luminescence line shapes of QDs with thousands of atoms. Our methodology was applied to the InP/ZnSe core/shell QDs and yielded a luminescence line shape that manifests remarkable agreement with the experiments. By analyzing HR factors, we revealed that exciton–acoustic phonon coupling dominantly determines the luminescence line shape for InP core-only QDs. Meanwhile, for the InP/ZnSe core/shell QDs, EPCs for both acoustic and optical modes similarly contribute to the line shape. The enhanced exciton–optical phonon coupling in the core/shell QD is attributed to uneven leakage of the HOMO and LUMO of the core to the shell region. With insights from the calculations, we suggested strategies to optimize the structure of the core/shell QDs. The results presented by this work allow for an in-depth understanding of EPCs and luminescence line shapes of QDs. Furthermore, our methodology can be applied to other QD systems of high current interest, such as perovskite QDs. Thus, we believe that this work will offer an opportunity to develop high-performance QDs.

■ ASSOCIATED CONTENT

ⓢ Supporting Information

The Supporting Information is available free of charge at https://pubs.acs.org/doi/10.1021/acsmaterialsau.1c00034.

Validation of approximations and methods (PDF)

■ AUTHOR INFORMATION

Corresponding Authors

Seungwu Han − *Department of Materials Science and Engineering and Research Institute of Advanced Materials, Seoul National University, Seoul 08826, Korea;* ⓞ orcid.org/0000-0003-3958-0922; Email: hansw@snu.ac.kr

Youngho Kang − *Department of Materials Science and Engineering, Incheon National University, Incheon 22012, Korea;* ⓞ orcid.org/0000-0003-4532-0027; Email: youngho84@inu.ac.kr

Author

Sungwoo Kang − *Department of Materials Science and Engineering and Research Institute of Advanced Materials, Seoul National University, Seoul 08826, Korea;* ⓞ orcid.org/0000-0001-8177-8815

Complete contact information is available at:
https://pubs.acs.org/10.1021/acsmaterialsau.1c00034

Notes

The authors declare no competing financial interest.

■ REFERENCES

(1) Steckel, J. S.; Snee, P.; Coe-Sullivan, S.; Zimmer, J. P.; Halpert, J. E.; Anikeeva, P.; Kim, L. A.; Bulovic, V.; Bawendi, M. G. Color-Saturated Green-Emitting QD-LEDs. *Angew. Chem., Int. Ed.* **2006**, *45* (35), 5796–5799.

(2) Eisler, H. J.; Sundar, V. C.; Bawendi, M. G.; Walsh, M.; Smith, H. I.; Klimov, V. Color-Selective Semiconductor Nanocrystal Laser. *Appl. Phys. Lett.* **2002**, *80* (24), 4614–4616.

(3) Yue, Z.; Lisdat, F.; Parak, W. J.; Hickey, S. G.; Tu, L.; Sabir, N.; Dorfs, D.; Bigall, N. C. Quantum-Dot-Based Photoelectrochemical Sensors for Chemical and Biological Detection. *ACS Appl. Mater. Interfaces* **2013**, *5* (8), 2800–2814.

(4) Peng, X.; Wickham, J.; Alivisatos, A. P. Kinetics of II-VI and III-V Colloidal Semiconductor Nanocrystal Growth: "Focusing" of Size Distributions. *J. Am. Chem. Soc.* **1998**, *120* (21), 5343–5344.

(5) Zhou, J.; Zhu, M.; Meng, R.; Qin, H.; Peng, X. Ideal CdSe/CdS Core/Shell Nanocrystals Enabled by Entropic Ligands and Their Core Size-, Shell Thickness-, and Ligand-Dependent Photoluminescence Properties. *J. Am. Chem. Soc.* **2017**, *139* (46), 16556–16567.

(6) Won, Y. H.; Cho, O.; Kim, T.; Chung, D. Y.; Kim, T.; Chung, H.; Jang, H.; Lee, J.; Kim, D.; Jang, E. Highly Efficient and Stable InP/ZnSe/ZnS Quantum Dot Light-Emitting Diodes. *Nature* **2019**, *575* (7784), 634–638.

(7) Kelley, A. M. Electron-Phonon Coupling in CdSe Nanocrystals. *J. Phys. Chem. Lett.* **2010**, *1* (9), 1296–1300.

(8) Salvador, M. R.; Graham, M. W.; Scholes, G. D. Exciton-Phonon Coupling and Disorder in the Excited States of CdSe Colloidal Quantum Dots. *J. Chem. Phys.* **2006**, *125* (18), 184709.

(9) Cui, J.; Beyler, A. P.; Coropceanu, I.; Cleary, L.; Avila, T. R.; Chen, Y.; Cordero, J. M.; Heathcote, S. L.; Harris, D. K.; Chen, O.; et al. Evolution of the Single-Nanocrystal Photoluminescence Linewidth with Size and Shell: Implications for Exciton-Phonon Coupling and the Optimization of Spectral Linewidths. *Nano Lett.* **2016**, *16* (1), 289–296.

(10) Gellen, T. A.; Lem, J.; Turner, D. B. Probing Homogeneous Line Broadening in CdSe Nanocrystals Using Multidimensional Electronic Spectroscopy. *Nano Lett.* **2017**, *17* (5), 2809–2815.

(11) Liptay, T. J.; Marshall, L. F.; Rao, P. S.; Ram, R. J.; Bawendi, M. G. Anomalous Stokes Shift in CdSe Nanocrystals. *Phys. Rev. B: Condens. Matter Mater. Phys.* **2007**, *76* (15), 155314.

(12) Kelley, A. M. Exciton-Optical Phonon Coupling in II-VI Semiconductor Nanocrystals. *J. Chem. Phys.* **2019**, *151* (14), 140901.

(13) Kang, S.; Kim, Y.; Jang, E.; Kang, Y.; Han, S. Fundamental Limit of the Emission Linewidths of Quantum Dots: An Ab Initio Study on CdSe Nanocrystals. *ACS Appl. Mater. Interfaces* **2020**, *12* (19), 22012–22018.

(14) Park, Y.-S.; Lim, J.; Klimov, V. I. Asymmetrically Strained Quantum Dots with Non-Fluctuating Single-Dot Emission Spectra and Subthermal Room-Temperature Linewidths. *Nat. Mater.* **2019**, *18* (3), 249−255.

(15) Protesescu, L.; Yakunin, S.; Bodnarchuk, M. I.; Krieg, F.; Caputo, R.; Hendon, C. H.; Yang, R. X.; Walsh, A.; Kovalenko, M. V. Nanocrystals of Cesium Lead Halide Perovskites (CsPbX$_3$, X = Cl, Br, and I): Novel Optoelectronic Materials Showing Bright Emission with Wide Color Gamut. *Nano Lett.* **2015**, *15* (6), 3692−3696.

(16) Behler, J.; Parrinello, M. Generalized Neural-Network Representation of High-Dimensional Potential-Energy Surfaces. *Phys. Rev. Lett.* **2007**, *98* (14), 146401.

(17) Blank, T. B.; Brown, S. D.; Calhoun, A. W.; Doren, D. J. Neural Network Models of Potential Energy Surfaces. *J. Chem. Phys.* **1995**, *103* (10), 4129−4137.

(18) Bartók, A. P.; Payne, M. C.; Kondor, R.; Csányi, G. Gaussian Approximation Potentials: The Accuracy of Quantum Mechanics, without the Electrons. *Phys. Rev. Lett.* **2010**, *104* (13), 136403.

(19) Lee, D.; Lee, K.; Yoo, D.; Jeong, W.; Han, S. Crystallization of Amorphous GeTe Simulated by Neural Network Potential Addressing Medium-Range Order. *Comput. Mater. Sci.* **2020**, *181*, 109725.

(20) Jeong, W.; Yoo, D.; Lee, K.; Jung, J.; Han, S. Efficient Atomic-Resolution Uncertainty Estimation for Neural Network Potentials Using a Replica Ensemble. *J. Phys. Chem. Lett.* **2020**, *11* (15), 6090−6096.

(21) Kang, S.; Jeong, W.; Hong, C.; Hwang, S.; Yoon, Y.; Han, S. Accelerated identification of equilibrium structures of multicomponent inorganic crystals using machine learning potentials. *arXiv*, **2021**, 2107.02594; https://arxiv.org/abs/2107.02594.

(22) Stoneham, A. M. *Theory of Defects in Solids*; Oxford University Press: Oxford, 1975.

(23) Alkauskas, A.; Lyons, J. L.; Steiauf, D.; Van De Walle, C. G. First-Principles Calculations of Luminescence Spectrum Line Shapes for Defects in Semiconductors: The Example of GaN and ZnO. *Phys. Rev. Lett.* **2012**, *109* (26), 267401.

(24) Alkauskas, A.; Buckley, B. B.; Awschalom, D. D.; Van de Walle, C. G. First-Principles Theory of the Luminescence Lineshape for the Triplet Transition in Diamond NV Centres. *New J. Phys.* **2014**, *16* (7), No. 073026.

(25) Huang, K.; Rhys, A. Theory of Light Absorption and Non-Radiative Transitions in F-Centres. *Proc. R. Soc. A* **1950**, *204* (1078), 406−423.

(26) Perdew, J. P.; Burke, K.; Ernzerhof, M. Generalized Gradient Approximation Made Simple. *Phys. Rev. Lett.* **1996**, *77* (18), 3865−3868.

(27) Dudarev, S.; Botton, G. Electron-Energy-Loss Spectra and the Structural Stability of Nickel Oxide: An LSDA+U Study. *Phys. Rev. B: Condens. Matter Mater. Phys.* **1998**, *57* (3), 1505−1509.

(28) Heyd, J.; Scuseria, G. E.; Ernzerhof, M. Hybrid Functionals Based on a Screened Coulomb Potential. *J. Chem. Phys.* **2003**, *118* (18), 8207−8215.

(29) Zang, X.; Lusk, M. T. Designing Small Silicon Quantum Dots with Low Reorganization Energy. *Phys. Rev. B: Condens. Matter Mater. Phys.* **2015**, *92* (3), No. 035426.

(30) Gavnholt, J.; Olsen, T.; Engelund, M.; Schiøtz, J. ΔSelf-Consistent Field Method To Obtain Potential Energy Surfaces of Excited Molecules on Surfaces. *Phys. Rev. B: Condens. Matter Mater. Phys.* **2008**, *78* (7), No. 075441.

(31) Togo, A.; Tanaka, I. First Principles Phonon Calculations in Materials Science. *Scr. Mater.* **2015**, *108*, 1−5.

(32) Lee, K.; Yoo, D.; Jeong, W.; Han, S. SIMPLE-NN: An Efficient Package for Training and Executing Neural-Network Interatomic Potentials. *Comput. Phys. Commun.* **2019**, *242*, 95−103.

(33) Jeong, W.; Lee, K.; Yoo, D.; Lee, D.; Han, S. Toward Reliable and Transferable Machine Learning Potentials: Uniform Training by Overcoming Sampling Bias. *J. Phys. Chem. C* **2018**, *122* (39), 22790−22795.

(34) Behler, J. Atom-Centered Symmetry Functions for Constructing High-Dimensional Neural Network Potentials. *J. Chem. Phys.* **2011**, *134* (7), No. 074106.

(35) Kingma, D. P.; Ba, J. L. Adam: A Method for Stochastic Optimization. *arXiv*, **2014**, 1412.6980; https://arxiv.org/abs/1412.6980.

(36) Plimpton, S. Fast Parallel Algorithms for Short-Range Molecular Dynamics. *J. Comput. Phys.* **1995**, *117* (1), 1−19.

(37) Carreras, A. *PhonoLAMMPS*, 2019; https://github.com/abelcarreras/phonolammps (accessed 2021-10-01).

(38) Lee, S. H.; Kim, Y.; Jang, H.; Min, J. H.; Oh, J.; Jang, E.; Kim, D. The Effects of Discrete and Gradient Mid-Shell Structures on the Photoluminescence of Single InP Quantum Dots. *Nanoscale* **2019**, *11* (48), 23251−23258.

(39) Jang, E.; Kim, Y.; Won, Y.-H.; Jang, H.; Choi, S.-M. Environmentally Friendly InP-Based Quantum Dots for Efficient Wide Color Gamut Displays. *ACS Energy Lett.* **2020**, *5* (4), 1316−1327.

(40) Kim, Y.; Ham, S.; Jang, H.; Min, J. H.; Chung, H.; Lee, J.; Kim, D.; Jang, E. Bright and Uniform Green Light Emitting InP/ZnSe/ZnS Quantum Dots for Wide Color Gamut Displays. *ACS Appl. Nano Mater.* **2019**, *2* (3), 1496−1504.

(41) Mortazavi, B.; Podryabinkin, E. V.; Roche, S.; Rabczuk, T.; Zhuang, X.; Shapeev, A. V. Machine-Learning Interatomic Potentials Enable First-Principles Multiscale Modeling of Lattice Thermal Conductivity in Graphene/Borophene Heterostructures. *Mater. Horiz.* **2020**, *7* (9), 2359−2367.

(42) Minamitani, E.; Ogura, M.; Watanabe, S. Simulating Lattice Thermal Conductivity in Semiconducting Materials Using High-Dimensional Neural Network Potential. *Appl. Phys. Express* **2019**, *12* (9), No. 095001.

(43) Mangold, C.; Chen, S.; Barbalinardo, G.; Behler, J.; Pochet, P.; Termentzidis, K.; Han, Y.; Chaput, L.; Lacroix, D.; Donadio, D. Transferability of Neural Network Potentials for Varying Stoichiometry: Phonons and Thermal Conductivity of Mn$_x$Ge$_y$ compounds. *J. Appl. Phys.* **2020**, *127* (24), 244901.

(44) Borcherds, P. H.; Alfrey, G. F.; Woods, A. D. B.; Saunderson, D. H. Phonon Dispersion Curves in Indium Phosphide. *J. Phys. C: Solid State Phys.* **1975**, *8* (13), 2022−2030.

(45) Hennion, B.; Moussa, F.; Pepy, G.; Kunc, K. Normal Modes of Vibrations in ZnSe. *Phys. Lett. A* **1971**, *36* (5), 376−378.